buildings

MDPI

Article

Structural Performance of Strengthening of High-Performance Geopolymer Concrete Columns Utilizing Different Confinement Materials: Experimental and Numerical Study

Aref A. Abadel

Department of Civil Engineering, College of Engineering, King Saud University, Riyadh 11421, Saudi Arabia; aabadel@ksu.edu.sa

Abstract: The objective of this study was to investigate the effectiveness of different confinement materials in strengthening geopolymer concrete (GP) columns subjected to axial compression loading. This research encompassed both experimental and numerical analyses. The experimental phase involved testing seven circular GP columns, while the numerical phase involved developing 3D finite element (FE) models using ABAQUS software. The primary focus of this study was to assess the impact of using outer and inner steel tubes, as well as an outer polyvinyl chloride (PVC) tube and a carbon-fiber-reinforced polymer (CFRP) sheet. To validate the FE models, the experimental results were utilized for comparison. The findings of this study revealed that the outer steel tube provided superior confinement effects on the GP column's concrete core compared to the PVC tube and CFRP sheet. The axial capacities of the columns confined with steel, PVC, and CFRP materials were observed to increase by 254.7%, 43.2%, and 186%, respectively, in comparison to the control specimens. Furthermore, the utilization of all confinement materials significantly enhanced the absorbed energy and ductility of the columns. The FE models demonstrated a reasonably close match to the experimental results in terms of load–displacement curves and deformation patterns. This correspondence between the numerical predictions and experimental data confirmed the reliability of the FE models and their suitability for generating further predictions. In summary, this study contributes to the field by exploring the efficacy of various confinement materials in strengthening GP columns. The results highlight the superior performance of the outer steel tube and demonstrate the positive influence of PVC and CFRP materials on enhancing the structural behavior of the columns. The validation of the FE models further supports their reliability and their potential for future predictions in similar scenarios.

Keywords: geopolymer concrete; CFST columns; CFRP sheet; PVC tube; inner steel tube; axial compressive loading; modeling

check for updates

Citation: Abadel, A.A. Structural Performance of Strengthening of High-Performance Geopolymer Concrete Columns Utilizing Different Confinement Materials: Experimental and Numerical Study. *Buildings* **2023**, *13*, 1709. https://doi.org/10.3390/buildings13071709

Academic Editor: Xiaoyong Wang

Received: 15 June 2023
Revised: 29 June 2023
Accepted: 29 June 2023
Published: 4 July 2023

1. Introduction

Concrete-filled steel tubes (CFST columns) are remarkable components in composite construction as they utilize the favorable qualities of both concrete and steel. The CFST columns, particularly circular ones, can stress concrete in a triaxial state due to confinement, resulting in better compression performance compared to an unconfined condition. However, concrete-filled steel tube (CFST) columns have gained significant attention in the concrete and steel composite construction field due to their ability to utilize the beneficial properties of both constituent materials effectively. Combining these materials can produce a robust structural member suitable for critical loading scenarios, offering improved stiffness, strength, and ductility. In circular CFST columns, the confinement effect plays a crucial role in enhancing the performance of concrete. When confined within the steel tube, concrete is subjected to triaxial stress, leading to higher compression performance than unconfined concrete [1,2]. This phenomenon occurs because the confinement restrains the lateral expansion of concrete, enabling it to withstand higher axial loads before failure. The presence of the steel tube also allows for the use of high-strength concrete by suppressing its explosive behavior [3,4]. High-strength concrete has the potential to exhibit brittle failure when subjected to high stress. Still, the steel tube in CFST columns restrains this behavior, leading to increased ductility and energy absorption capacity [1,5,6]. Overall, CFST columns offer numerous advantages over traditional concrete or steel columns, such as enhanced load-carrying capacity, improved ductility, greater resistance to buckling, and better fire resistance [2,7,8].

Geopolymer concrete (GC) is a sustainable [9,10], eco-friendly construction material that has garnered significant attention in recent years due to its exceptional mechanical properties and durability [11–15]. GC is made from an alkali-activated binder system consisting of industrial by-products such as fly ash and metakaolin, significantly reducing cement production's environmental impact [16,17]. Fly ash is a by-product of coal combustion in power plants, while metakaolin is a thermally activated kaolinite clay [18]. These materials are widely used in the production of geopolymer concrete due to their pozzolanic and reactive properties, which contribute to the formation of a dense, strong, and durable matrix [19–21]. Several studies have examined the behavior of ambient-cured geopolymer concrete structures reinforced with steel or FRP composite bars [22–24]. These experiments show that reinforced geopolymer concrete columns have limited ductility and brittle failures [11]. After reaching their maximal loads, these columns can lose up to 90% of their resistance [25]. Concrete-filled steel tubes (CFSTs) can improve ductility and structural performance [24,26,27]. Fiber-reinforced cementitious matrix (FRCM) was also used as confinement by Combers et al. [28] to enhance the strength of concrete cylinders. Another study by Alrashoudi et al. [22] utilized different strengthening schemes to enhance the axial capacity of geopolymer concrete. All these strengthening schemes improve the axial strength and ductility of concrete structures successfully.

In the last twenty years, there has been a growing trend toward enhancing the compressive performance of structural members to keep up with cutting-edge engineering advancements [20,29–32]. Different strengthening configuration using FRP strengthening system has been studied [33–35]. Recently, concrete-filled columns have gained significant attention in the recent literature due to their efficient combination of reduced weight, exceptional bending stiffness, and superior cyclic performance [36,37]. The columns' stiffness and strength can be further improved by utilizing ultra-high-strength concrete to fill the space between the inner and outer steel tubes [38]. The presence of ultra-high-strength concrete inside the column helps to delay or prevent buckling of the outer steel tube, while the outer steel tube effectively confines the concrete core. Columns with double concrete-filled tubes offer enhanced fire resistance compared to single concrete-filled tube columns, as the outer steel tube and shell concrete protect the inner steel tube [39–42]. These double-filled columns have attracted considerable attention in the form of experimental and numerical studies due to their advantageous engineering properties [43,44]. Despite the considerable benefits these double-section columns bring to composite construction, there is a notable scarcity of quantitative evaluations for such members in the existing literature [45,46].

When circular columns of geopolymer concrete (GC) with fly ash and metakaolin are subjected to axially loaded conditions, they exhibit several key characteristics [22,47]. Firstly, due to the high compressive strength of GC, these columns can withstand substantial axial loads without significant deformation. Additionally, the confinement effect provided by the circular cross-section enhances the concrete's load-carrying capacity and ductility. The less porous and denser geopolymer matrix than traditional concrete offers increased resistance to environmental factors that may otherwise lead to premature failure [48]. Furthermore, fly ash and metakaolin form a robust and cohesive binder system that improves overall durability [49]. Finally, it is important to note that the column's load-carrying capacity can be further enhanced via steel reinforcement, such as by creating fiber-reinforced concrete (FRC) or concrete-filled steel tubes (CFST), depending on the specific design requirements and loading scenarios [50]. Ozbakkaloglu and Xie [51] tested 36 square fiber-reinforced polymer tubes with concrete under axial compression. These examples were made with OPC or fly ash-based geopolymer concrete. Composite column compressive strength was rarely affected by concrete type. Geopolymer concrete columns had lower ultimate axial strain than OPC reference samples. Shrinkage caused the stress–strain curves of OPC columns to plateau in the transition zones. Since geopolymer concrete shrank less, its curves did not have a plateau.

In a study conducted by Shi et al. [25], an experimental investigation was carried out on square cross-section columns filled with geopolymeric recycled concrete and steel. The researchers compared the test results with those of columns made of cement-based recycled aggregate concrete. The compressive strengths of both types of concrete were similar during testing. However, the geopolymer CFST columns exhibited 23~26% higher load-carrying capacities compared to the cement-based CFST columns when no recycled aggregate was used. When 50% or 100% natural coarse aggregate was replaced with recycled aggregate, both geopolymer and cement-based CFST columns had comparable load-carrying capacities. Another notable finding from Shi et al.'s [25] research was that the geopolymer CFST columns had smaller peak strains at peak loads compared to their cement-based CFST counterparts.

The existing literature reveals a scarcity of data concerning enhancing compressive behavior in axially loaded, concrete-filled circular columns using various confinement materials. Furthermore, although the behavior of concrete-filled circular columns has been investigated, no experimental studies have been carried out on geopolymer-concrete (GC)-filled circular columns subjected to axial loads. Additionally, no numerical analyses have been conducted on GC-filled circular columns under axial compression. To fill this research gap, this study aims to assess the influence of different confinement materials and inner steel tubes on the axial compression properties of GC-filled circular columns. The significance of this study lies in the potential benefits of GC-filled circular columns for composite construction, warranting further research to expand and reinforce the existing knowledge base on this subject.

2. Experimental Study Procedure

2.1. Materials and GP Mixture

2.1.1. GP Concrete

The test columns were cast using geopolymer concrete that was based on a 1:1 mixture of MK and FA. This ratio was chosen to balance the geopolymer's fresh and hardened characteristics without using heat curing. Additionally, Zhang et al.'s research demonstrated that this ratio was ideal for producing compressive and bending strengths at room temperature and upon exposure to high temperatures [52]. Table 1 provides the chemical composition of MK and FA. The alkali activator utilized consisted of a 14 M sodium hydroxide solution for all mixes and a sodium silicate solution with a silicate modulus of 3.1 ($SiO_2/Na_2O = 3.1$). The coarse aggregate in the mixture was a natural limestone and ranged in size from 5 to 10 mm. The fine aggregate in this study was a combination of crushed limestone aggregates and white sand, with sizes ranging from 1 to 5 mm. In this investigation, a single GP concrete mixture was used. The proportions of the GP concrete mixture that was used to cast each test specimen are shown in Table 2. The dry materials (aggregates and metakaolin) were thoroughly blended to create GP concrete. Then, an alkaline solution (a mixture of NaOH and Na_2SiO_3) was added, and the mixing continued for a few minutes. Then, GP concrete was poured into column molds and tubes. After 28 days of curing, the GP mixture was designed to have a compressive strength of 30 MPa.

Table 1. MK's and FA's chemical composition (% wt).

Material	CaO	Al_2O_3	SiO_2	Fe_2O_3	MgO	K_2O	P_2O_5	Na_2O	SO_3	Others
MK	1.29%	42.63%	51.00%	2.11%	0.13%	0.34%	0.05%	0.28%	0.44%	1.74%
FA	0.28%	24.80%	61.30%	4.39%	0.74%	1.49%	0.45%	0.12%	0.39%	6.06%

Table 2. GP concrete mixture proportions (kg/m^3).

Components	Quantities
MK	214
Fly ash	143
White Sand	403
Fine agg.	170
Coarse agg.	1220
Water Glass	285
NaOH	105

2.1.2. Steel Tube

Figure 1 depicts the steel tube (i.e., the steel circular hollow section) used in this present experimental study. The mild steel tubes had a yield strength of 285 MPa when tested in tension in accordance with ASTM-E8 [53]. The steel tubes' axial load–displacement curve under axial compression is depicted in Figure 2.

Figure 1. Steel tubes used in this study.

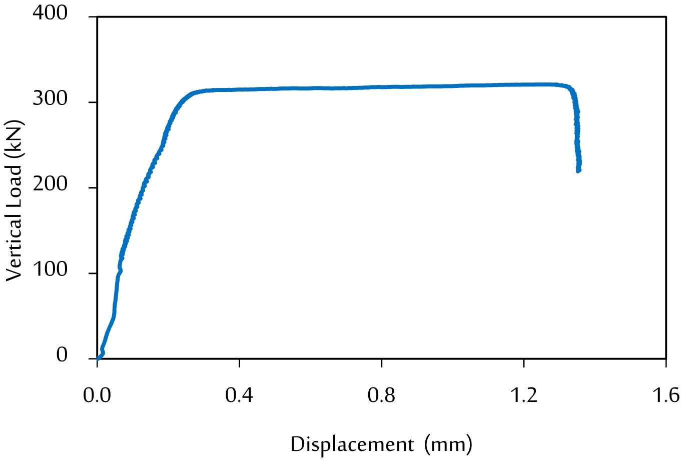

Figure 2. The steel tube's experimental load–displacement curve used in this study [27].

2.1.3. CFRP Sheet

Table 3 displays the properties of the carbon fibers used for specimen strengthening. Data were obtained using flat coupon testing in accordance with ASTM D3039 [54]. For strengthened specimens (i.e., GP-CFRP specimens), the columns were wrapped using epoxy-impregnated CFRP sheet in a hoop-like pattern after a very thin coating of epoxy resin was brushed onto the concrete columns.

Table 3. The sieve analysis results of the sand.

Sieve No. (mm)	Passing, %	Iraqi Specification, IQS No. 45
4 (4.75)	91	90–100
8 (2.36)	83	75–100
16 (1.18)	74.8	55–90
30 (0.6)	57.2	35–59
50 (0.3)	24.2	8–30
100 (0.15)	7.2	0–10

2.1.4. PVC Tube

The PVC pipes were used as confinement schemes to manufacture the GP-PVC specimens, which were available commercially. The PVC pipes were manufactured for water purposes with a nominal pressure of 4.1 MPa according to ASTM D1785 [48]. As shown in Figure 3, the selected PVC pipe has a wall thickness of 3 mm and a diameter of 110 mm. For the purpose of measuring the compressive properties of the PVC tubes used in the GP-PVC specimens, a few hollow PVC tube specimens were tested under axial compression. The global and local elephant foot buckling were the causes of PVC tube failure, as seen in Figure 3. Figure 4 shows the axial load–displacement curve of the PVC tubes put through testing while being compressed axially. Table 4 lists the material characteristics of the PVC tubes.

(**a**) (**b**)

Figure 3. Deformation patterns in PVC tubes: (**a**) global bulging; (**b**) local elephant foot buckling.

Table 4. CFRP properties.

Material	Ultimate Tensile Strength (MPa)	Tensile Modulus of Elasticity (GPa)	Ultimate Tensile Strain	Thickness (mm)
CFRP sheet	1122	68.9	1.7%	1

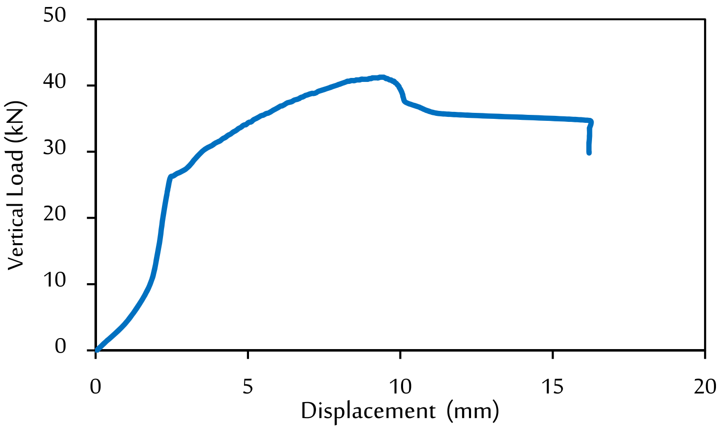

Figure 4. The PVC tube's experimental load–displacement curve used in this study [27].

2.2. Test Specimens

Seven GP circular columns' behavior has been tested experimentally, which were set up to be investigated under axial compression loading. The Con-GP specimen (i.e., control column) had a 106 mm diameter and was 300 mm long. The other specimens' diameters, however, varied depending on the confinement scheme based on the confinement scheme; for GP-CFST, GP-PVC, and GP-CFRP columns, respectively, it was 106 mm, 106 mm, and 102 mm. Table 5 gives the specifics of the circular columns. Letter strings with dashes between them represent the specimen IDs. The letter string Con refers to the control specimen; concrete-filled steel tube is referred to as CFST; S refers to solid columns without an inner confinement scheme; Ann refers to columns with an inner confinement scheme; PVC refers to PVC tube confinement at the outer diameter of columns; CFRP refers to the wrapping of a concrete column with CFRP sheet. A cross-section of all columns tested in this study is shown in Figures 5–7. The first specimen (i.e., Con-GP) was the control column in this study. As shown in Table 5, the second and third columns (GP-CFST-S and GP-CFST-Ann) were utilized for investigating the influence of steel tubes on the improvement of the compressive capacity of columns under axial loading (see Figure 5). GP-PVC-S and GP-PVC-Ann, the fourth and fifth columns, were used to investigate the influence of utilizing PVC tubes as outer confinement, as shown in Figure 6. The sixth and seventh columns, GP-CFRP-S and GP-CFRP-Ann, were designed to investigate the strengthening of the control columns using CFRP sheets (see Figure 7).

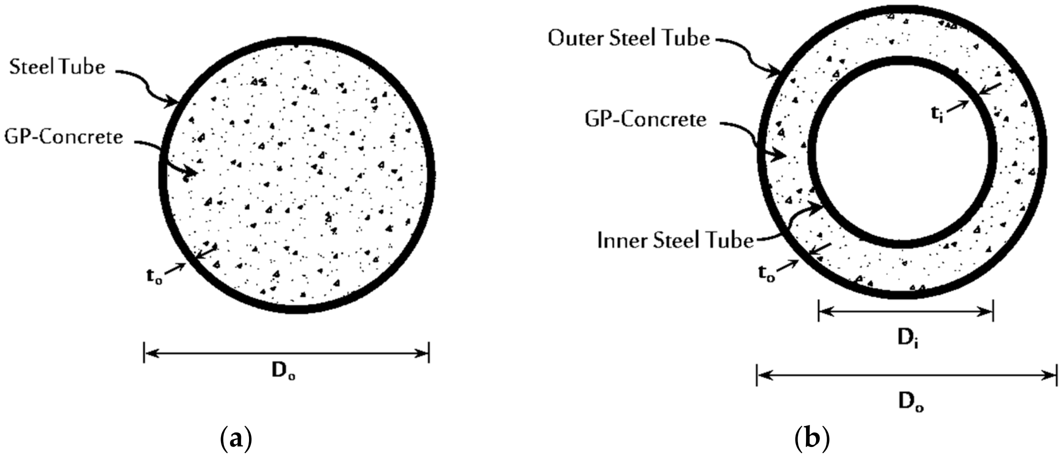

Figure 5. GP-CFST specimens: (**a**) GP-CFST-S; (**b**) GP-CFST-Ann.

Table 5. Details of the column tested in this study.

Specimen ID	Confinement Type	Confinement Schemes	Inner Steel Tube		Outer Tube	
			D_i (mm)	t_i (mm)	D_o (mm)	t_o (mm)
GP-Con	Control	-	-	-	-	-
GP-CFST-S	Steel	Confinement of the outer surface using steel tube.	-	-	106	3
GP-CFST-Ann	Steel	Confinement of the outer and inner surfaces using steel tubes.	60	5	106	3
GP-PVC-S	PVC	Confinement of the outer surface using PVC tube.	-	-	106	3
GP-PVC-Ann	PVC	Confinement of the outer surface using PVC tube and the inner surface using steel tube.	60	5	106	3
GP-CFRP-S	CFRP-wrapped	Confinement of the outer surface using one CFRP sheet layer.	-	-	102	1
GP-CFRP-Ann	CFRP-wrapped	Confinement of the outer surface using one CFRP sheet layer and the inner surface using steel tube.	60	5	102	1

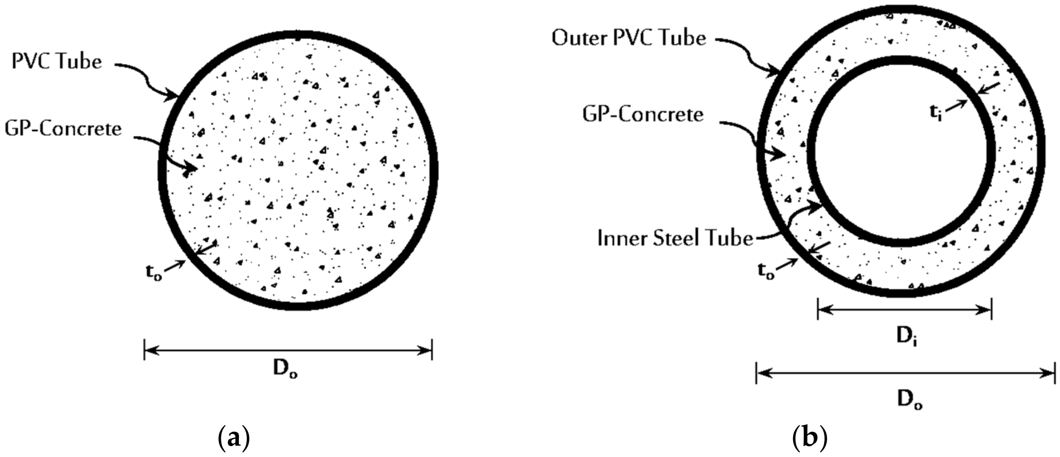

Figure 6. GP-PVC specimens: (**a**) GP-PVC-S; (**b**) GP-PVC-Ann.

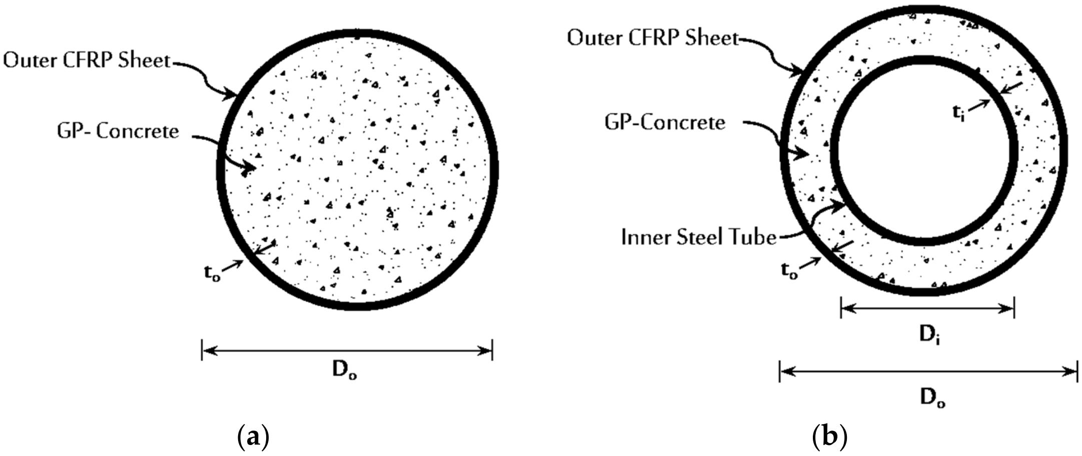

Figure 7. GP-CFRP specimens: (**a**) GP-CFRP-S; (**b**) GP-CFRP-Ann [27].

2.3. Specimen Preparation

All of the specimens were cast, cured, strengthened, and tested in the structural laboratory at King Saud University. The steel tubes and the hollow PVC pipe were meticulously cut to lengths of about 300 mm in order to take a subsequent strengthening procedure into account. In order to possibly apply uniform axial pressure to the specimens' upper surface, the top and bottom surfaces of the steel tubes were later formed perpendicular to the tube's axis and flat. A crucial component for achieving an accurate assessment result is the leveled column ends [55,56]. After going through the forming procedure, the steel tubes' exact final length was 300 mm. The interior and exterior surfaces of the steel tubes were meticulously cleaned to ensure that any dust or residues are entirely removed and that the concrete and steel tubes will come into the best possible contact. At the bottom surfaces of the tube sections (i.e., steel and PVC), flat, thick wood plates were placed to support the concrete during the casting processes. As depicted in Figure 8, silicon was utilized to connect the wood plates to the bottom surfaces of the hollow sections. After that, concrete was cast into the tubes and formwork. To reduce the possibility of compaction issues in the narrow shell and core areas of the different tubes, the casting procedure was meticulously carried out. The concrete surface was polished with a steel trowel after being cast to level the top surfaces of the columns. According to ACI-308R-01-R08 [57], the formwork was removed after 24 h, and the columns were moist cured for 28 curing days at lab temperature. First, water was misted onto the concrete surfaces. After that, burlap was used to cover the specimen. The burlap was then wet twice daily for the following few days. The CFRP wrap was placed manually via a wet layup process. Then, an epoxy-resin-soaked CFRP sheet was wrapped around the column surfaces. In order to avoid direct loading from the loading machine, the CFRP sheet has been wrapped along its entire length except for 5 mm from the two bottom surfaces of the GP-CFRP-S and GP-CFRP-Ann specimens. Prior to implementing the strengthening schemes, the surfaces of the specimens (i.e., GP-CFRP-S and GP-CFRP-Ann) were roughened using sandblasting to create an effective bond between the CFRP sheet and the core concrete surfaces. Before implementing CFRP jacketing, the surfaces of the concrete core were lightly scraped to eliminate the surface dust, and the dust was completely removed. In order to fill air gaps and create a solid bond, an epoxy primer coating was put on the exterior concrete core surface. Next, a very thin epoxy coat was applied to the concrete surfaces. The CFRP layer was then carefully wrapped after that. Making sure there were no air voids between the concrete's surface and the CFRP sheet was crucial. All specimens are shown in Figure 9 before testing.

Figure 8. Supporting the columns using wood plates before casting.

Figure 9. Specimens before testing.

2.4. Testing Setup and Instrumentation

The specimens were compressed after 28 days of curing using a universal testing machine (UTM) with 1000 kN. Testing has been conducted via displacement control at a loading rate of 0.5 mm/min. Before the test, the two ends of the columns were leveled using a concrete end grinder to ensure an even distribution of the axial load on the column surface. In order to capture the attained load and displacement as well as the specimens' strain, a data acquisition unit has been used throughout each test. For each of the specimens, two vertical linear variable differential transformers (LVDTs) were installed at mid-height around the columns' perimeter to capture the deformation between the gauge lengths of 200 mm, as shown in Figure 10. For capturing axial strains in the loading process and revising LVDT readings earlier in the loading procedure, all specimens were equipped with two unidirectional strain gauges at mid-height, as shown in Figure 10. This is due to the fact that a resultant slack in the test setup frequently leads to inaccurate early-stage LVDT measurements. To measure the hoop strain of the PVC tube or the strain in the CFRP sheet, two uniformly dispersed, unidirectional strain gauges were installed at mid-height outside the designated overlap area.

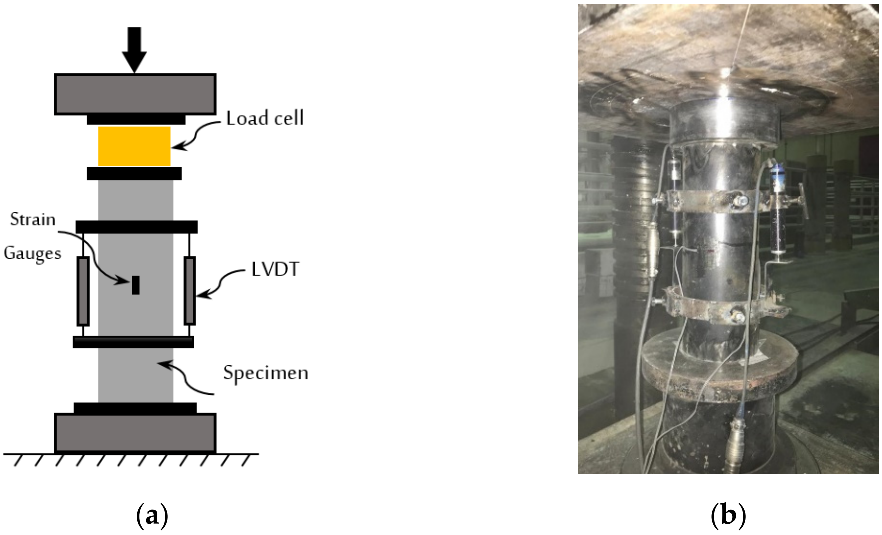

Figure 10. Instrumentation and test settings: (**a**) instrumentation arrangement; (**b**) columns ready for testing.

3. Results and Discussion

Concrete cylinders for the GP mix were created in accordance with ASTM C31 [58] (diameter: 100 mm; height: 200 mm). Table 6 shows the mechanical characteristics of the GP mixture, including the compressive and splitting tensile strengths according to ASTM

C39 [59] and ASTM C496 [60], respectively. The average compressive strength was 32 MPa with a standard division of 1.1, and the average splitting tensile strength was 3.8 MPa with a strand division of 0.9. Three specimens of each test were used. Alkaline activators and FA particles are joined to sodium aluminosilicate hydrate gel (N-A-S-H), the dominant phase, via polymerization. Strong linkages within polymer chains are only possible because of the polymerization of silica in the FA to create geopolymer chains [61].

Table 6. The mechanical properties of the GP mix.

Concrete Mix	Compressive Strength (f_c')	Splitting Tensile Stress
GP concrete	32 MPa	3.8 MPa

3.1. Mode of Failure

Failure modes of all the specimens are shown in Figure 11. The failure mechanisms of the specimens show the individual and composite physical behavior of various columns' components (i.e., confinement materials). The displayed failure mode of the column is a combination of steel yielding and concrete crushing under compression. However, the failure's behavior was impacted by the characteristics of the inner and outer tubes. As demonstrated in Figure 11a, the control column's failure mode (i.e., GP-Con) was concrete crushing via shear, splitting, and then failing abruptly, such as a conventional concrete cylinder. According to Figure 11b, the lower edge of the concrete-filled steel column (i.e., GP-CFST-S) exhibited local buckling, which is connected to the plasticization of this area. The composite columns also have the advantage of preventing shear failure modes with the presence of an outer steel tube in the GP-CFST-S column. The outer steel tube must have performed a good composite activity in order for the steel tube and concrete to function properly together. Achieving this harmony in composite structural parts is very important [27,55]. The failure mode of the inner steel tube in relation to the GP-CFST-Ann column is shown in Figure 11c. As seen in Figure 11c, the inner steel tube has exhibited an excessive degree of inner local buckling, which was caused by the lack of internal support against the inward local buckling compared with GP-CFST. This degree of severe local buckling prevents exploiting the yield capability of the inner steel tube of the GP-CFST-Ann column. Additionally, this local buckling problem would affect the effectiveness of the shell concrete. This indicates that the concrete core and inner steel tube in this situation would not be able to cooperate properly. The PVC wall bulged and deformed dramatically when the PVC tubes were used (i.e., GP-PVC-S), as the concrete in the core expanded, pushing the PVC wall outwards, as shown in Figure 11d. The inner steel tube in the PVC specimen (i.e., the GP-PVC-Ann) had an excessive degree of inward local buckling as for the GP-CFST-Ann specimen, as seen in Figure 11e. The concrete's crushing and dilatation created an energy that the PVC tube could not effectively absorb. The GP-CFRP-S column failed in an abrupt and explosive manner. According to Figure 11f, the ringed rupture in the top sections of the GP-CFRP-S specimen occurred as a result of the significant dismantling of the CFRP sheet from the concrete's perimeter. Figure 11f shows the rupture of the CFRP sheet in the upper half of the GP-CFRP-S column. The similar circumstance for the GP-CFRP-S specimen and the presence of the inner steel tube both caused an excessive degree of inward local buckling for the GP-CFRP-Ann specimen with a gap, as illustrated in Figure 11g. Debonding failure has happened concurrently with the CFRP fracture because the bond's strength was inadequate to withstand the hoop's tensile force once the CFRP ruptured, which was caused by the radial expansion. According to the findings, the debonding failure was not observed prior to the CFRP's fracture, which may be attributable to the localized effects of concrete shrinkage since evaporation can only happen on the top surface [62].

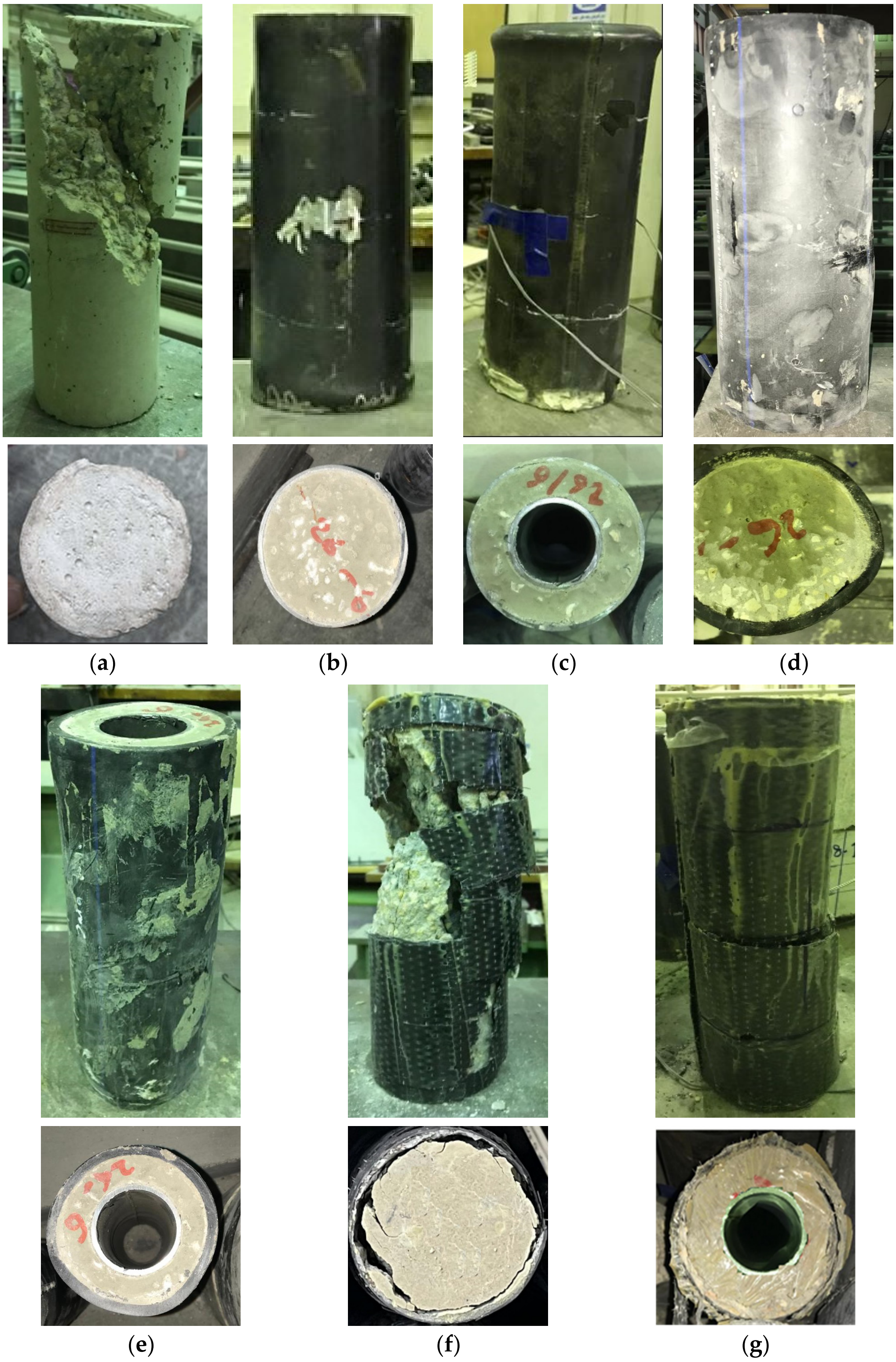
(**a**) (**b**) (**c**) (**d**)

(**e**) (**f**) (**g**)

Figure 11. Failure modes of all specimens: (**a**) GP-Con; (**b**) GP-CFST-S; (**c**) GP-CFST-Ann; (**d**) GP-PVC-S; (**e**) GP-PVC-Ann; (**f**) GP-CFRP-S; (**g**) GP-CFRP-Ann.

3.2. Load–Displacement Characteristics

Figure 12 shows the load versus displacement curves of all columns. Generally, the load–displacement curves are composed of three phases: the linear first phase is when the concrete core and tubes behave elastically and the load increases linearly; the second phase indicates transitional nonlinear segments of the curves, while the third phase represents the softening segments. Due to concrete cracking and the tube's local buckling, the slope of the load–displacement curves started to decrease and display nonlinear behavior. For the GP-Con specimen, the axial load increased until the first peak load value and displayed a sharp decline in the axial load due to concrete crushing via shear, splitting, and failing abruptly. Additionally, the GP-CFST-S and GP-CFST-Ann columns behaved similarly, with a slight reduction in the axial load for the GP-CFST-Ann compared with the GP-CFST-S. As seen in Figure 12, GP-CFST-S and GP-CFST-Ann columns (i.e., columns with steel tubes) have a higher load capacity than the other specimens. Additionally, the presence of the outer steel tube in the GP-CFST-S and GP-CFST-Ann columns developed more ductility compared with all specimens (based on the area under the load–displacement curves). The concrete-filled PVC tube columns (GP-PVC-S and GP-PVC-Ann) behaved similarly, with a significant reduction in the softening segments (i.e., less ductility) of the load–displacement for the GP-PVC-Ann compared with the GP-PVC-S, as shown in Figure 12. Regarding the specimens with CFRP wrapping, the load-carrying capability and ductility of the GP-CFRP-S and GP-CFRP-Ann columns were extremely similar. The CFRP rupture was the cause of the abrupt decrease in load-carrying capacity depicted in Figure 12. Table 7 summarizes the testing results for the specimens. The axial stress of the specimens can be determined by dividing the axial load by the cross-section area of the specimens (taking into account the outer diameters of the various confinement methods). The maximum axial load capacity was obtained in the GP-CFST-S specimen with an increased ratio of 254.67%, 7.49%, 147.7%, 230.6%, 23.9%, and 30.5% compared with GP-Con, GP-CFST-Ann, GP-PVC-S, GP-PVC-Ann, GP-CFRP-S, and GP-CFRP-Ann, respectively. The results showed an obvious superiority for the use of steel tubes as a confinement material for concrete core, followed by the use of the CFRP sheet, then the PVC tube in the last place, as illustrated in Table 7. However, GP-PVC-S and GP-PVC-Ann showed increased ratios compared with the control column (i.e., GP-Con) of 43.2% and 7.3%, respectively, which is an acceptable increase compared to the economic aspect. The use of inner steel tubes in columns led to decreased axial load values. The reported reduction ratios were 6.9%, 25.1%, and 5.0% for GP-CFST-Ann, GP-PVC-Ann, and GP-CFRP-Ann, respectively, compared with GP-CFST-S, GP-PVC-S, and GP-CFRP-S, which can be attributed to the numerous cycles of local buckling that occurred in the inner steel tubes. The specimens' ductility performance should also be taken into consideration in order to conduct a thorough examination. The ductility performance may be predicated on the compression loading response of the specimens' end-shortening curves (i.e., post-peak behavior). The enhanced ductility behavior can be indicated by a higher degree of end shortening at the maximum load capacity. On the other hand, the less ductile specimens exhibited a descending portion after achieving the maximum load capacities at reduced end shortening values. The GP-CFST-S and GP-CFST-Ann specimens exhibit high ductility compared with other specimens, as shown in Figure 12. The presence of the outer steel tube has performed a good composite activity, allowing the steel tube and concrete to function properly together, which led to enhanced specimens' ductility performances. In addition, GP-CFRP-S and GP-CFRP-Ann exhibited poor ductility compared to their counterparts with PVC outer tubes. The ringed rupture in the top sections of the CFRP sheet caused an abrupt and explosive failure, which limited the development of the ductility of the CFRP specimen. Although the concrete GP-PVC-Ann shows a 7.3% increase in ratio axial load capacity compared with the control column (i.e., GP-Con), it showed a significant increase in ductility performance. PVC tubes, despite producing less confinement, distributed stress caused by the expansion of the concrete core, reducing stress concentration due to asymmetrical cracking, which improved the ductility performance. Due to the unconfined concrete's brittleness, Figure 12 clearly shows that the ductility of the unstrengthened specimens is noticeably lower than that of the strengthened specimens. Here, it is important to underline the outer tube's dominant involvement in the ductility behavior of the specimens. Comparisons of the ductility of unstrengthened specimens (i.e., control specimens) and strengthened specimens lead to an important conclusion.

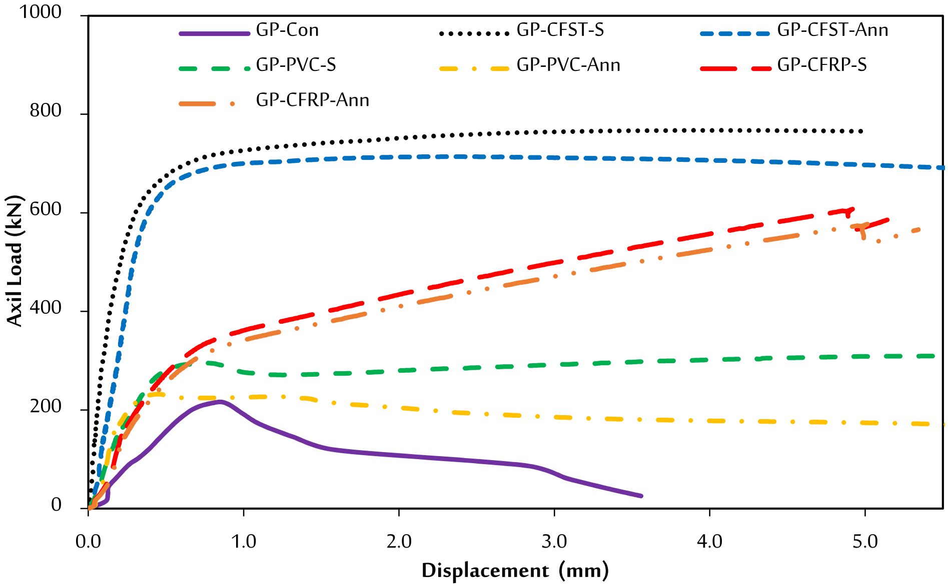

Figure 12. Load versus displacement curves of all columns.

Table 7. Test findings for all tested columns.

Column ID	GP-Con	GP-CFST-S	GP-CFST-Ann	GP-PVC-S	GP-PVC-Ann	GP-CFRP-S	GP-CFRP-Ann
Axial Load (kN)	216.45	767.69	714.19	309.87	232.19	619.13	588.17
Stress (MPa)	27.57	87.04	119.15	32.62	34.80	75.81	110.12
Displacement at peak (mm)	0.851	3.892	2.283	5.573	0.448	5.614	5.705
Axial strain	0.00426	0.01946	0.01142	0.02787	0.00224	0.02807	0.02853
Transverse strain	−0.00354	−0.01246	−0.01372	−0.00319	−0.00148	−0.00231	−0.00243

3.3. Stress–Strain Curves

Under the effects of axial compression pressure, the specimens' concrete cores began to crack. The confinement materials are put under lateral stress when the concrete dilates after it fractures. The axial pressure produced by the concrete core as well as hoop/transverse stresses led to it pushing outward against the various confinement walls. The various confinement walls (i.e., steel tube, PVC tube, and CFRP sheet) were subjected to biaxial pressure, and the concrete itself was subjected to triaxial constraint due to the confinement walls. The axial and transverse strain values and the stress results were combined to create the stress–strain curves, as depicted in Figure 13. At the middle point height of various confinement types, the specimens' strain values were measured using axial (longitudinal) and transverse strain gauges. Throughout the initial loading phase, all strains increased linearly. Transverse/hoop strains on confinement walls during the elastic stage were remarkably low, as shown in Figure 13. This can be attributed to the fact that the axial compression load could be carried through the concrete core and confinement walls without any expansion in the concrete core. The strains on the outside various confinement walls gradually achieved yield strains as the load increased. When the stresses reached their maximum, the slope of the stress–strain curves began to decline, and almost all strain values surpassed the yield strain limitations. The findings show the use of different confinement components effectively supports the concrete core and improves the bearing capacity of the specimens. As shown in Table 7, the highest axial strains were recorded in the CFRP-wrapped columns (i.e., GP-CFRP-S and GP-CFRP-Ann); this can be attributed to the fact that the CFRP sheet usually fails in rupture without allowing large transverse deformations. Nevertheless, the highest transverse strains were recorded in the CFST columns (i.e., GP-CFRP-S and GP-CFRP-Ann) as a result of the steel tubes providing further confinement for the concrete core. Although it produced comparatively less confinement, PVC tubes provided a specific mechanism that evenly distributed the stress caused by the expansion of the concrete core, hence lowering the stress concentration due to the concrete being cracked asymmetrically [63,64]. The GP-CFST-Ann column had the maximum level of stress, as seen in Figure 13 and Table 7, compared to all other columns. The GP-CFST-S, GP-CFST-Ann, and GP-CFRP-Ann columns, therefore, experienced much more stress than any other specimen, proving that the confinement materials in those specimens generated more confinement strength prior to total failure. The findings demonstrated that, in comparison to the provided outer PVC tube and the CFRP sheet wrapped, the outer steel tube provided a greater confinement strength on the concrete core. Although the annular columns (i.e., GP-CFST-Ann, GP-PVC-Ann, and GP-CFRP-Ann) had smaller cross-sectional areas than the remaining columns (i.e., GP-Con, GP-CFST-S, GP-PVC-S, and GP-CFRP-S), the annular columns showed higher stress (up to 45.3%) than the remaining columns as a result of the presence of inner steel tubes. When the load level exceeded the maximum limits, the concrete expanded as a result of axial compression pressure, which enhanced the interaction between the two components. Additionally, the enhanced interaction has caused a rapid increase in the transverse strain and a reduction in the axial stress near the midpoint of the steel tube.

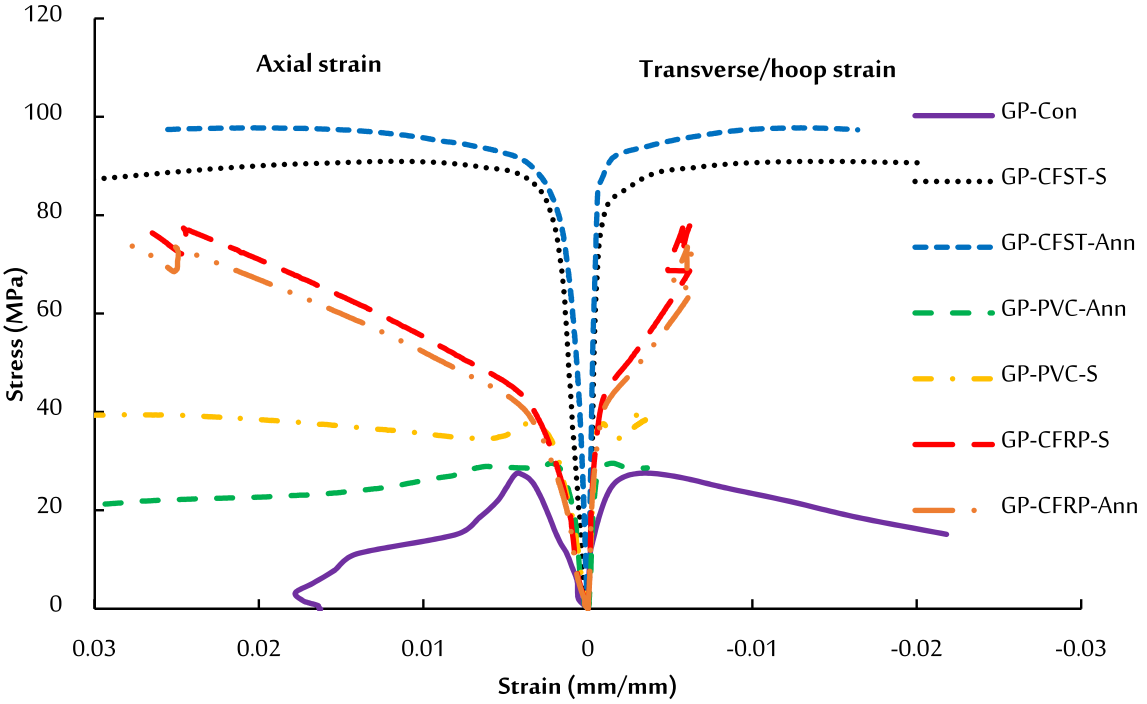

Figure 13. The axial and transverse strain–stress curves in all specimens.

4. Finite Element Type

The obtained experimental results were validated using FE analysis. The nonlinear FE models were created using the ABAQUS software [65]. A single step was used to conduct an FE analysis of all specimens in the ABAQUS-Explicit.

4.1. Finite Element Type

Continuum solid cube elements (i.e., C3D8R) were used to model the concrete core, as well as steel and PVC tubes. For the CFRP sheet, shell elements (i.e., S4R) were used. Figure 14 shows the element types used for all the columns in this study.

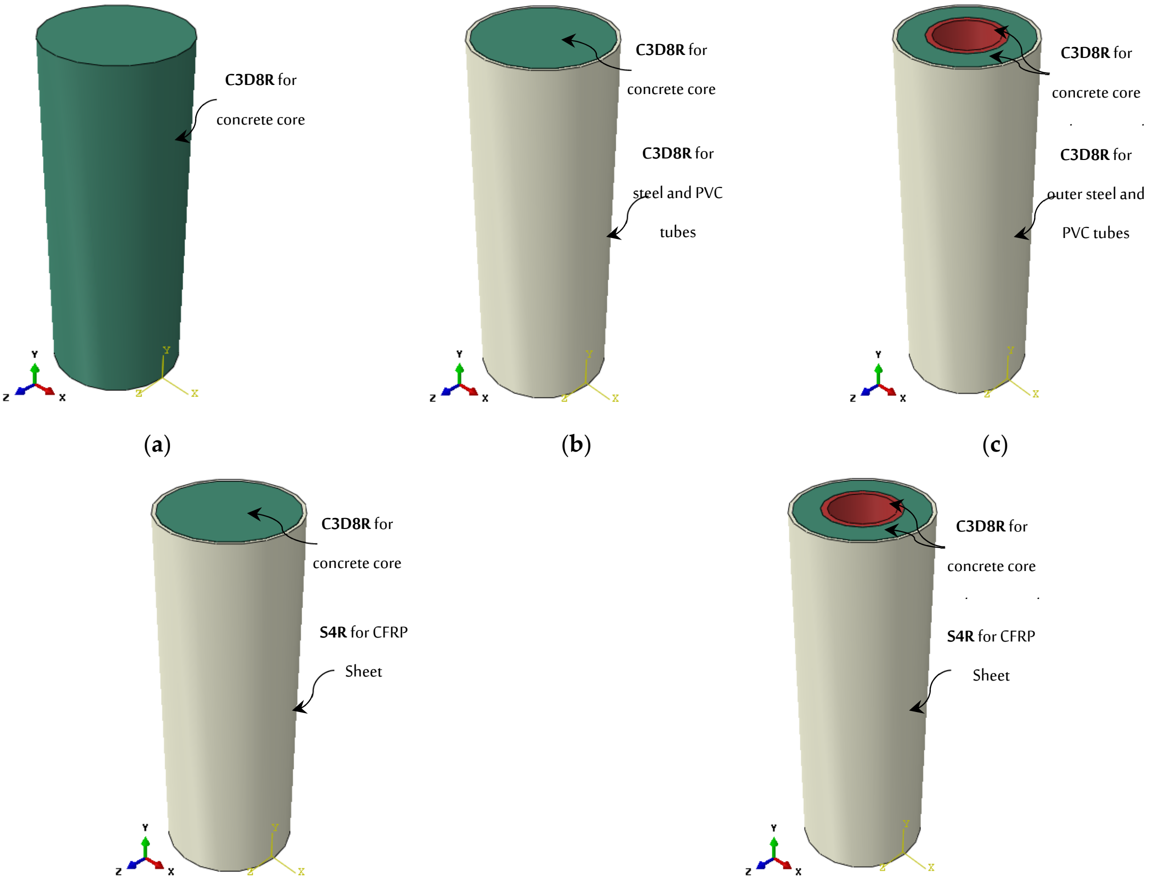

(**a**) (**b**) (**c**)

(**d**) (**e**)

Figure 14. Three-dimensional model of the FE columns: (**a**) GP-Con column; (**b**) GP-CFST/ PVC-S columns; (**c**) GP-CFST/ PVC-Ann columns; (**d**) GP-CFRP-S column; (**e**) GP-CFRP-Ann column.

4.2. Boundary Conditions and Loading Application

The axial compression loading was applied as a downward vertical displacement (i.e., displacement control) at the top surface of the columns, as shown in Figure 15b. The material density of all members was defined to simulate the members' self-weight via the application of a gravity load in the ABAQUS software. As shown in Figure 15b, all degrees of freedom (i.e., DOFs) were restricted (i.e., fixed support) to the specimen's bottom surface.

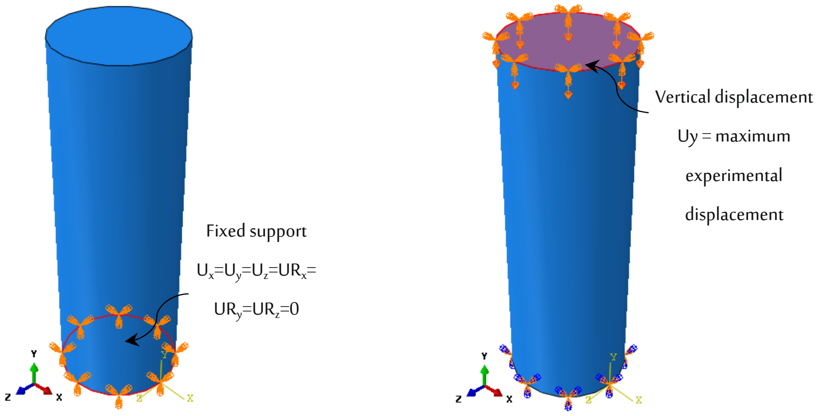

(**a**) (**b**)

Figure 15. Columns' loading and boundary conditions (**a**) at fixed support (**b**) at fixed support and loading surface.

4.3. Material Modeling

Table 8 summarizes the mechanical characteristics of all the materials used in the FE model, including the GP concrete and confinement materials (i.e., PVC, steel, and CFRP). According to Sharif et al. [66], the unconfined concrete characteristics created via the current experimental test (i.e., a compressive test of the concrete cylinder) need to be transformed into a confined stress–strain curve created by [63]. In this study, the concrete plasticity was modeled using the concrete damaged plasticity model (CDPM) from Lubliner et al. [67] and Lee and Fenves [68], which is currently available in ABAQUS and is widely used in FE modeling (e.g., REF). The parameters σ_{b0}/σ_{c0} and K_c in CDPM were set to 1.16 and 0.7, respectively. Additionally, the eccentricity parameter (ϵ) and dilation angle (ψ) were defined as 0.10 and 38°, respectively. The splitting tensile strengths from Section 3.1 were used to compute the maximum tensile strength of concrete (σ_{ct}), which is shown in Figure 16. As illustrated in Figure 16, the crack bandwidth (h_{cr}) and fracture energy (G_f) were used to define the softening component, and the area under the softening segment was calculated by dividing the G_f by the h_{cr}. For the GP concrete in this study, G_f was calculated based on CEB-FIP Code [69] using the following Equation:

$$G_f = 0.03\left(\frac{f'_c}{10}\right)^{0.7} \tag{1}$$

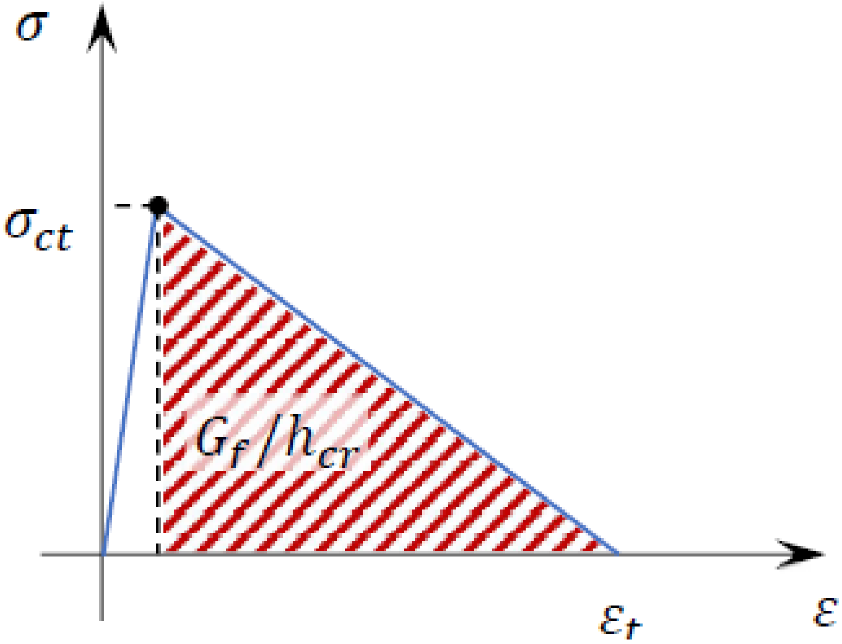

Figure 16. Tensile model of GP the concrete.

The steel material properties have been simulated as a nonlinear plastic model in order to accurately reflect the behavior actually based on the experimental results. In order to model the PVC's plastic characteristics in the ABAQUS software, the experimental load–displacement curve (see Figure 4) was transformed into a stress–strain curve. The results of the experiment showed that tensile rupture caused the failure of the CFRP sheet. Regarding the CFRP composite, laminate modeling was used in the ABAQUS software. The testing results showed the strongest tensile strength in the direction of the fibers, whereas other strength values were low and were taken based on [27,70,71].

Table 8. Mechanical characteristics of the concrete, steel, PVC, and CFRP used in the FE models.

Material	Parameters	Values	Denotation
Concrete	Poisson′s ratio (v)	0.15	Widely used in FE modeling
	Modulus of Elasticity (E)	26,587.2 MPa	$(E = 4700\sqrt{f'_c})$ ACI 318M-11 [72]
	Dilation angle (ψ)	38°	Calibrated value
	Flow potential eccentricity (ϵ)	0.1	ABAQUS (default value) [73]
	Ratio of biaxial to uniaxial compressive $(\sigma_{b0}/\sigma_{c0})$	1.16	ABAQUS (default value) [73]
	Second stress invariant ratio (K_c)	0.7	ABAQUS (default value) [73]
Steel	Poisson′s ratio (v)	0.3	Widely used in FE modeling
	Modulus of Elasticity (E)	200,000 MPa	Widely used in FE modeling
	Yield stress (σ_y)	285 MPa	Experimental Value
	Ultimate stress (σ_u)	406 MPa	Experimental Value
PVC	Poisson′s ratio (v)	0.38	Widely used in FE modeling
	Modulus of Elasticity (E)	3000 MPa	Wang and Yang [74]
	Tensile yield strength (σ_y)	45 MPa	Wang and Yang [74]
CFRP sheet	Poisson′s ratio (v)	0.3	Widely used in FE modeling
	Tensile strength (longitudinal: σ_{t1})	1122 MPa	Experimental Value
	Modulus of Elasticity (E)	230,000 MPa	Given by the manufacturer
	Transversal tensile strength (σ_{t2})	10 MPa	Al-Mekhlafi et al. [73]
	Compressive strength (longitudinal: σ_{c1})	10 MPa	
	Compressive strength (transversal: σ_{c2})	10 MPa	
	Shear strength (longitudinal: τ_{f1})	10 MPa	
	Shear strength (transversal: τ_{f2})	10 MPa	

4.4. Modelling of FE Contacts

To represent the binding between the concrete core and the CFRP sheet, the modeling has been carried out as a tie interaction. The interactions between the tubes (i.e., steel and PVC) and the concrete core were simulated via tangential behavior utilizing a friction interaction. The friction coefficient for the concrete inside the steel tube was 0.25 [63,73], while it was 0.08 for the concrete inside the PVC tube, which was widely used in FE modeling. In addition to the tangential behavior, hard contact was utilized to simulate contact in the conventional direction.

4.5. Meshing Convergence

A mesh convergence study utilizing two types of mesh densities (i.e., size 10 and size 5) was carried out exclusively on the GP-Con specimen, as shown in Figure 17. The geometry, element types, and material properties for the two regular mesh densities were all the same. To choose which mesh size to use, the two mesh sizes were evaluated. The mesh density of 5 was chosen due to requiring reasonable computational time while still producing results that possess the greatest accuracy and convergence in relation to experimental data. A mesh density of more than 5 did not improve the accuracy significantly, and further refinement of the mesh efforts cost more time and resources while having longer running times. The columns were all given the same size as a result.

4.6. FE Modeling Validation

Using the ABAQUS software to analyze the FE model under an axial compression load, the failure modes (stress contour plots) of columns were produced. Figures 18–24 illustrate the experimental versus numerical failure modes of all specimens in more detail. The predicted deformation forms and stress plots of the FE models are reasonably similar to the experimental observations. To further evaluate the FE models' reliability, their maximum load capacity and value load–displacement curves were obtained, which were utilized for comparison against the results of experimental tests. Accordingly, Figure 25 compares the load–displacement curves of FE models and experimental columns. In the elastic segment, as shown in Figure 25, the FE column curves exhibited good agreement compared with the experimental results. Generally, both curves shared a similar overall pattern. The stiffness and ductility of the test columns were evaluated computationally and experimentally over the entire range of responses, as shown in Figure 25. The FE models, using constitutive modeling, can be observed to clearly predict the descending portion of the load–displacement curves (see Figure 25). Table 9 shows the maximum load capacities of all of the columns' FE and experimental tests. It should be highlighted that FE models produce findings that are higher than experimental test results. This can be noticed in the GP-PVC-Ann and GP-CFRP-Ann, which showed increased ratios of 10.50% and 11.08% compared with experimental results, respectively. In addition, the GP-CFST-S exhibited a reduction of 3.59% compared with experimental results. Moreover, the GP-CFRP-S specimens exhibited a great fit, as the difference ratio was only 1.48%. However, the largest discrepancy between the FE and the experimental results in terms of maximum load capacities, as shown in Table 9, was around 11%. There was typically little relative inaccuracy in the FE results. Due to the columns' typically perfect behavior throughout the FE modeling, which caused less damage to the FE models than to the experimental columns, there were deviations in some of the secant stiffness segments of the FE curves. Furthermore, several factors might be related to the resulting difference in ultimate load capacities and load–displacement curves. For example, the early weaknesses in the concrete, including nonuniformity, degradation, and early cracks, were not appropriately assessed in the FE modeling. Ultimately, the modeling results substantially supported the reliability of the FE models, making them acceptable for generating additional predictions.

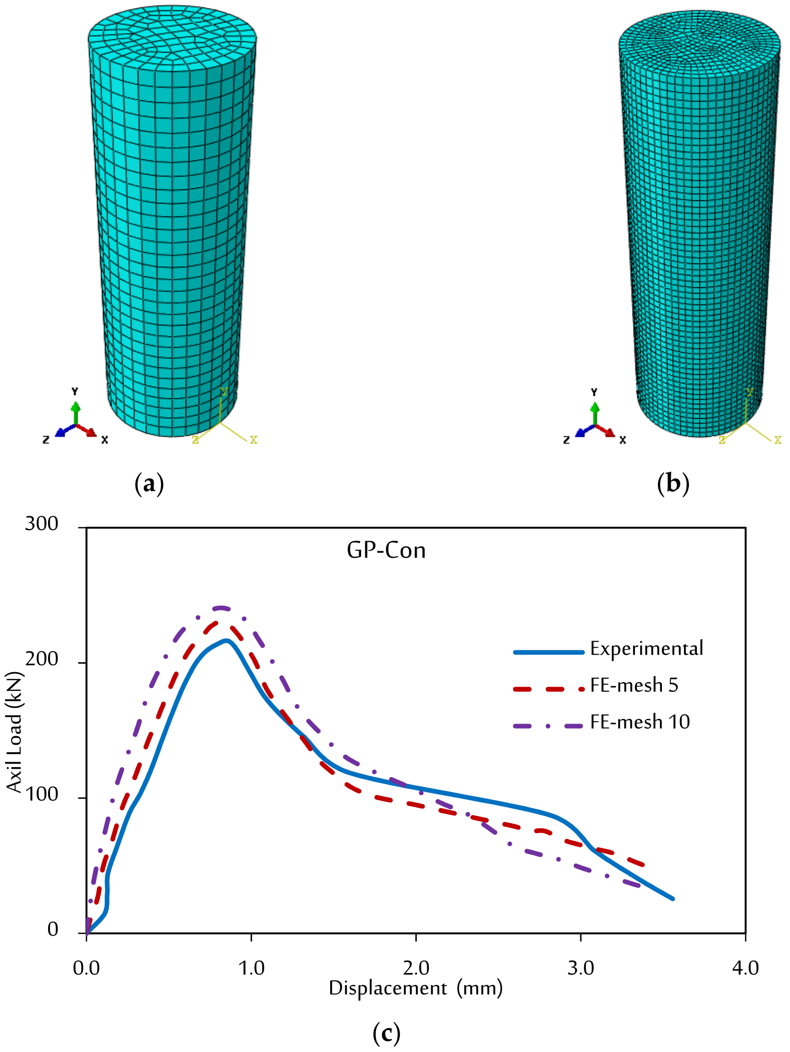

(**a**)

(**b**)

(**c**)

Figure 17. FE mesh convergence study: (**a**) size 10; (**b**) size 5; (**c**) mesh convergence result.

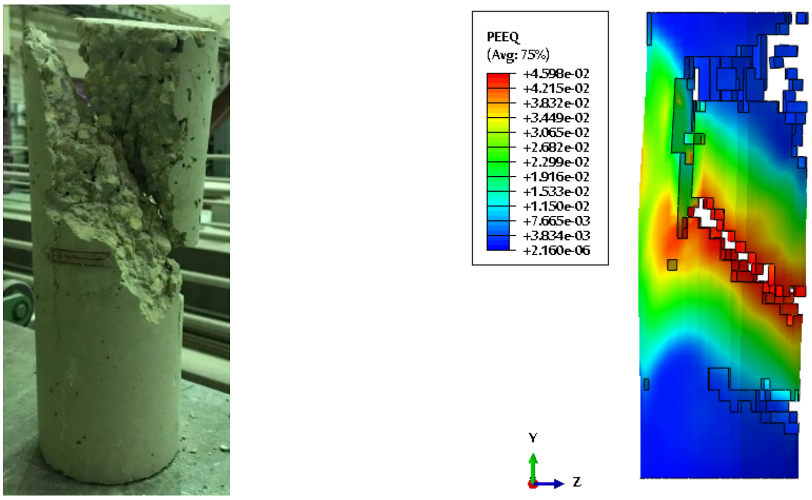

Figure 18. Experimental versus numerical failure modes of the GP-Con specimen.

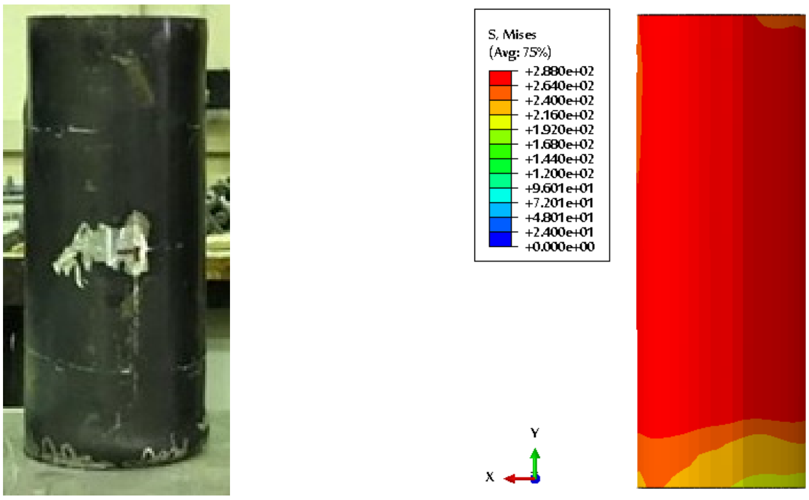

Figure 19. Experimental versus numerical failure modes of the GP-CFST-S specimen.

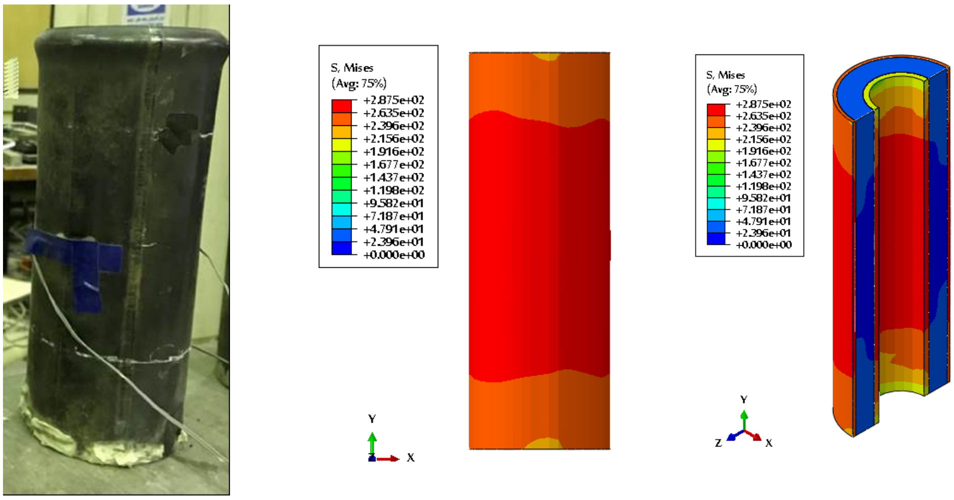

Figure 20. Experimental versus numerical failure modes of the GP-CFST-Ann specimen.

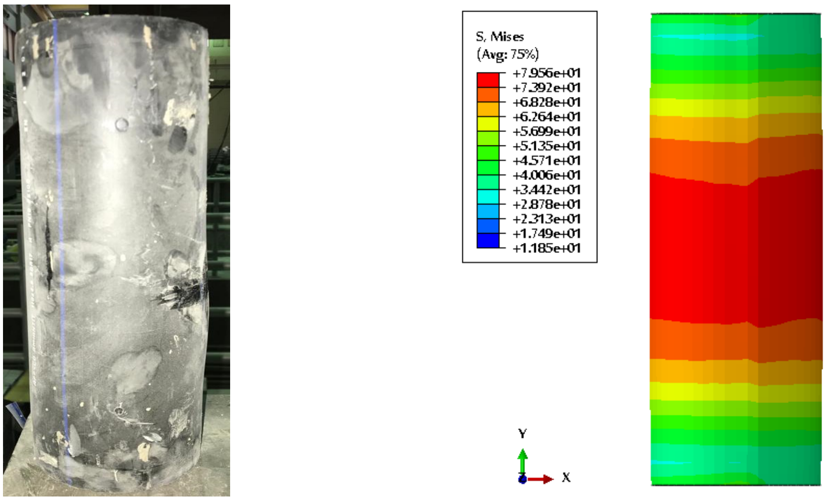

Figure 21. Experimental versus numerical failure modes of the GP-PVC-S specimen.

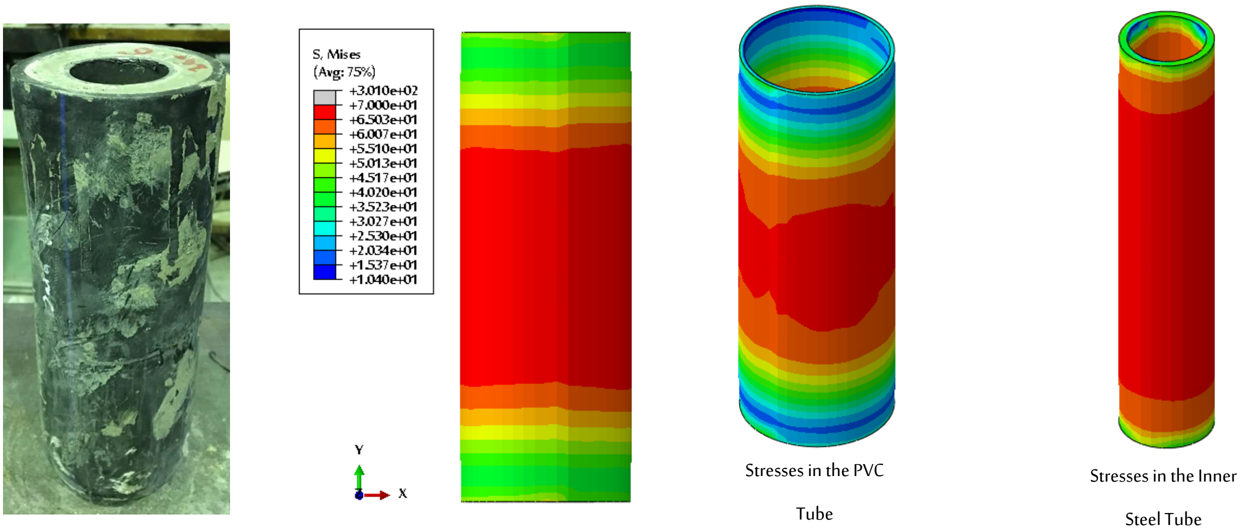

Figure 22. Experimental versus numerical failure modes of the GP-PVC-Ann specimen.

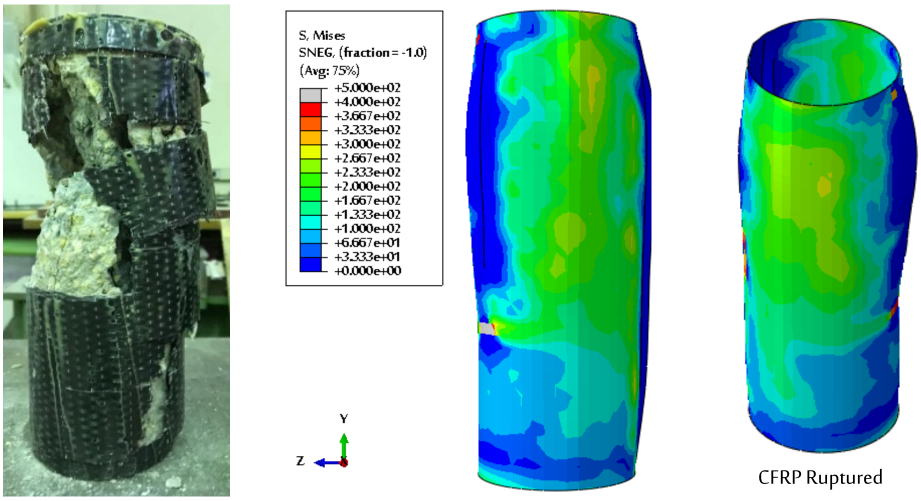

Figure 23. Experimental versus numerical failure modes of the GP-CFRP-S specimen.

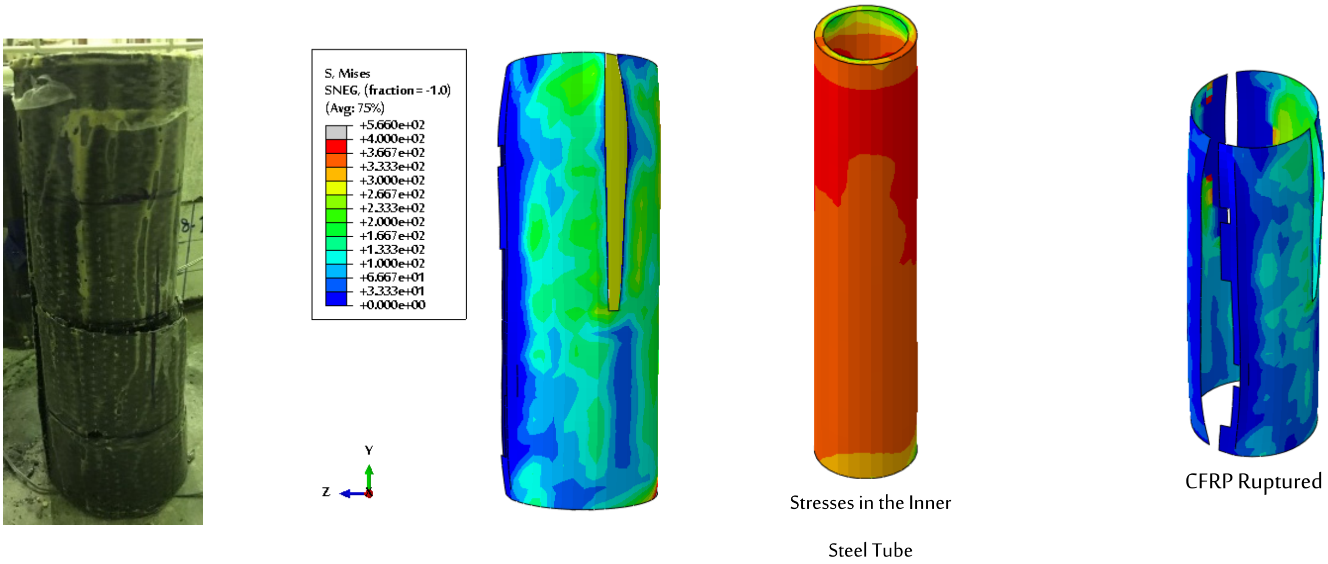

Figure 24. Experimental versus numerical failure modes of the GP-CFRP-Ann specimen.

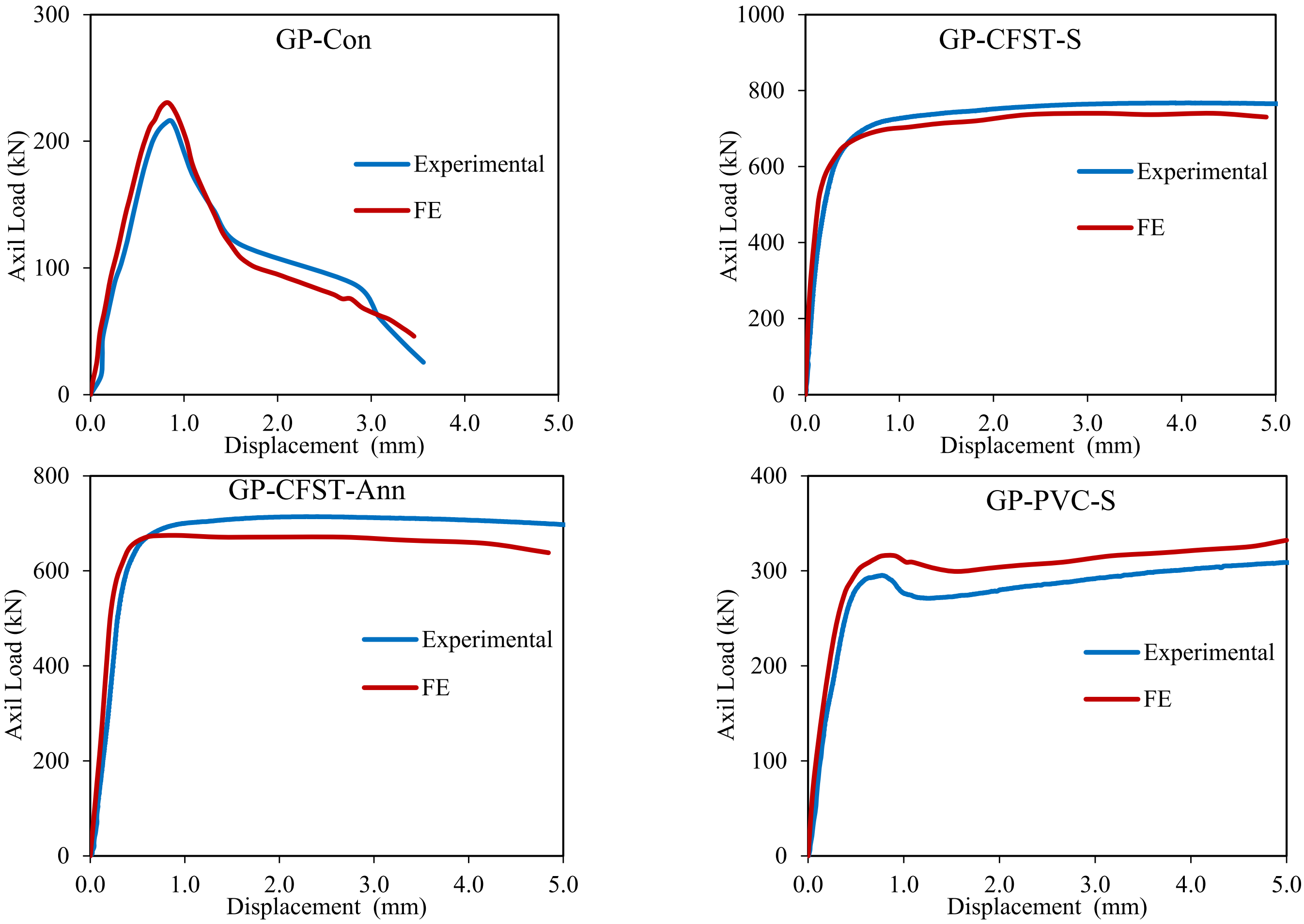

Figure 25. *Cont.*

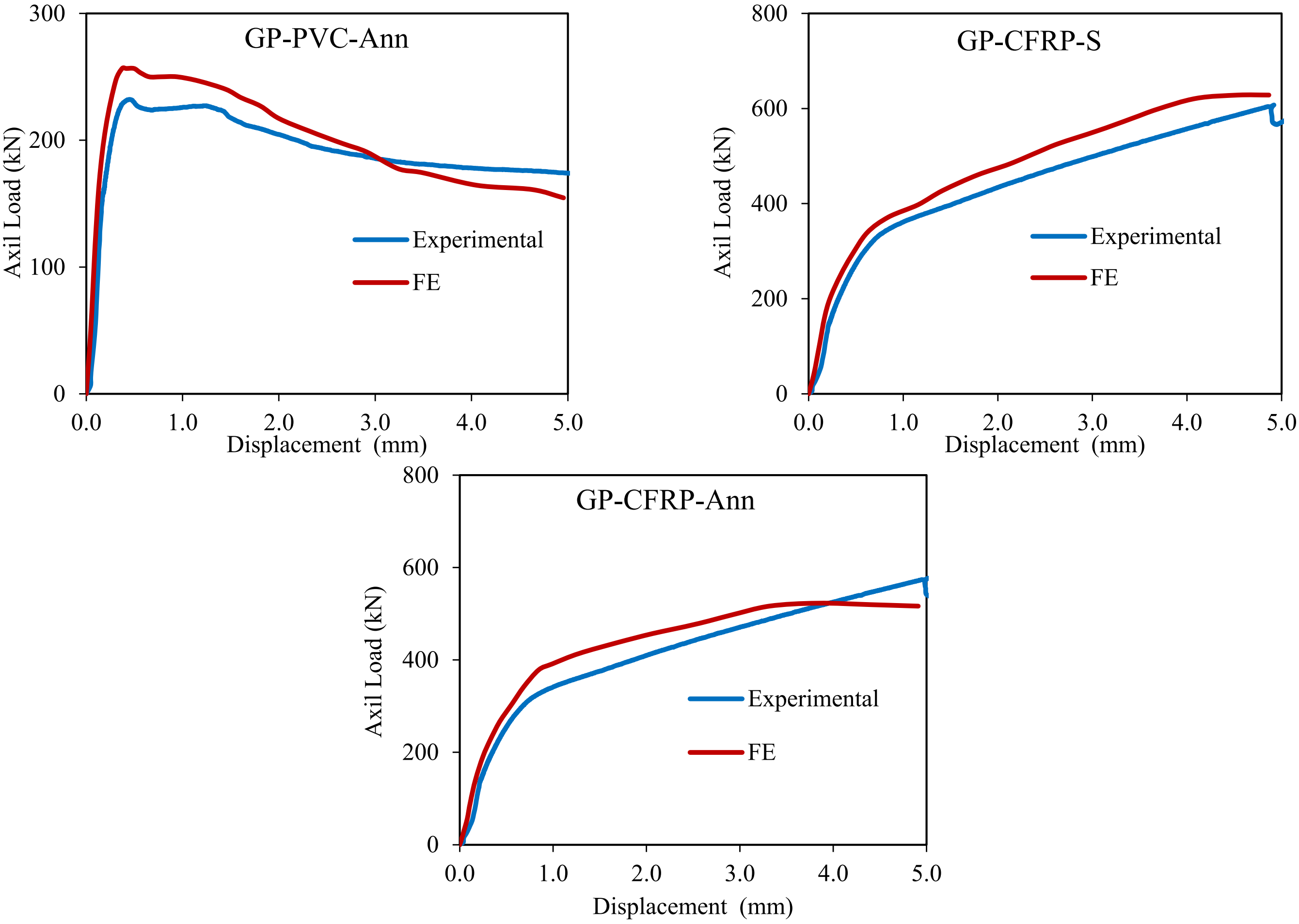

Figure 25. All specimens' experimental and FE load–displacement curves.

Table 9. Comparing the maximum load capacities of FE and experimental results.

Column ID	GP-Con	GP-CFST-S	GP-CFST-Ann	GP-PVC-S	GP-PVC-Ann	GP-CFRP-S	GP-CFRP-Ann
Experimental Load P_{Exp} (kN)	216.45	767.69	714.19	309.87	232.19	619.13	588.17
FE Load P_{FE} (kN)	230.26	740.13	674.34	332.24	256.58	628.29	523.03
$P_{FE}/P_{Exp.}$	1.06	0.96	0.94	1.07	1.11	1.01	0.89
Error %	+6.38%	−3.59%	−5.58%	+7.22%	+10.50%	+1.48%	−11.08%

5. Conclusions

Several conclusions can be drawn from the results of this experimental and FE study, including the following:

1. The outer steel tube had a higher confinement influence on the concrete core compared to the PVC tube and CFRP sheet. The CFST column exhibited the greatest axial strength capacity, with a ratio increase of up to 254.7%.
2. Inward local buckling of the inner steel tube was observed in all specimens, impacting the effectiveness of the concrete core and resulting in an underutilized yield capacity for the inner steel tube.
3. The inclusion of inner steel tubes decreased the axial load capabilities of the columns. Compared to GP-CFST-S, GP-PVC-S, and GP-CFRP-S, the decreased ratios for GP-CFST-Ann, GP-PVC-Ann, and GP-CFRP-Ann were 6.9%, 25.1%, and 5.0%, respectively.
4. PVC tubes, despite producing less confinement, distributed stress caused by the expansion of the concrete core, reducing stress concentration due to asymmetrical cracking. However, the substantial deformation and bulging of PVC tubes made it

challenging to absorb a sufficient amount of energy from the crushing and dilatation of the concrete core.

5. The failure of the GP-CFRP-S specimen showed an abrupt and explosive nature. A CFRP fracture on the compression edge was the primary cause of the failure. The ringed rupture of the GP-CFRP-S column is related to the delamination of a substantial CFRP layer from the concrete surface.
6. The predicted deformation forms and load–displacement curves of the FE models are reasonably similar to the experimental results. The modeling results substantially supported the reliability of the FE models, making them acceptable for generating additional predictions.

The authors believe that additional research should be conducted in order to identify novel approaches for enhancing CFST columns in exposure circumstances. However, this investigation contributes to the knowledge by providing designers, specialists, and researchers with useful information on the performance of the GC-filled tube columns under axially loaded tests. More research is needed to investigate the effect of some parameters, such as the column slenderness ratio, pipe sizes, and the number of CFRP layers. Additionally, various loading configurations, such as the lateral load, fire exposure, and size effect, need to be well examined.

Funding: The authors extend their appreciation to Researchers Supporting Project number (RSP2023R343), King Saud University, Riyadh, Saudi Arabia.

Data Availability Statement: The data that support the findings of this study are available from the corresponding author upon reasonable request.

Conflicts of Interest: The author declares no conflict of interest.

References

1. Liu, Z.; Lu, Y.; Li, N.; Zong, S. Experimental investigation and computational simulation of slender self-stressing concrete-filled steel tube columns. *J. Build. Eng.* **2022**, *48*, 103893. [CrossRef]
2. Khan, M.; Chu, S.H.; Deng, X.W.; Wang, Y. Protection of steel tube against corrosion using self-prestressing UHPC prepared with expansive agent and steel fibers. *Structures* **2022**, *37*, 95–108. [CrossRef]
3. Abadel, A.; Abbas, H.; Almusallam, T.; Alshaikh, I.M.H.; Khawaji, M.; Alghamdi, H.; Salah, A.A. Experimental study of shear behavior of CFRP strengthened ultra-high-performance fiber-reinforced concrete deep beams. *Case Stud. Constr. Mater.* **2022**, *16*, e01103. [CrossRef]
4. Raouf, S.; Ibraheem, O.; Tais, A. Confinement effectiveness of CFRP strengthened concrete cylinders subjected to high temperatures. *Adv. Concr. Constr.* **2020**, *9*, 7. [CrossRef]
5. Zhou, X.; Mou, T.; Tang, H.; Fan, B. Experimental Study on Ultrahigh Strength Concrete Filled Steel Tube Short Columns under Axial Load. *Adv. Mater. Sci. Eng.* **2017**, *2017*, 8410895. [CrossRef]
6. Xu, L.; Lu, Q.; Chi, Y.; Yang, Y.; Yu, M.; Yan, Y. Axial compressive performance of UHPC filled steel tube stub columns containing steel-polypropylene hybrid fiber. *Constr. Build. Mater.* **2019**, *204*, 754–767. [CrossRef]
7. Fan, W.; Shen, D.; Zhang, Z.; Huang, X.; Shao, X. A novel UHPFRC-based protective structure for bridge columns against vehicle collisions: Experiment, simulation, and optimization. *Eng. Struct.* **2020**, *207*, 110247. [CrossRef]
8. Heniegal, A.M.; Maaty, A.A.E.S.; Agwa, I.S. Simulation of the behavior of pressurized underwater concrete. *Alex. Eng. J.* **2015**, *54*, 183–195. [CrossRef]
9. Jiang, X.; Zhang, Y.; Zhang, Y.; Ma, J.; Xiao, R.; Guo, F.; Bai, Y.; Huang, B. Influence of size effect on the properties of slag and waste glass-based geopolymer paste. *J. Clean. Prod.* **2023**, *383*, 135428. [CrossRef]
10. Althoey, F.; Zaid, O.; Alsulamy, S.; Martínez-García, R.; de Prado-Gil, J.; Arbili, M.M. Experimental study on the properties of ultra-high-strength geopolymer concrete with polypropylene fibers and nano-silica. *PLoS ONE* **2023**, *18*, e0282435. [CrossRef]
11. Liu, Y.; Zhang, Z.; Shi, C.; Zhu, D.; Li, N.; Deng, Y. Development of ultra-high performance geopolymer concrete (UHPGC): Influence of steel fiber on mechanical properties. *Cem. Concr. Compos.* **2020**, *112*, 103670. [CrossRef]
12. Liu, Y.; Shi, C.; Zhang, Z.; Li, N.; Shi, D. Mechanical and fracture properties of ultra-high performance geopolymer concrete: Effects of steel fiber and silica fume. *Cem. Concr. Compos.* **2020**, *112*, 103665. [CrossRef]
13. Ghosh, R.; Sagar, S.P.; Kumar, A.; Gupta, S.K.; Kumar, S. Estimation of geopolymer concrete strength from ultrasonic pulse velocity (UPV) using high power pulser. *J. Build. Eng.* **2018**, *16*, 39–44. [CrossRef]
14. Ambily, P.S.; Ravisankar, K.; Umarani, C.; Dattatreya, J.K.; Iyer, N.R. Development of ultra-high-performance geopolymer concrete. *Mag. Concr. Res.* **2014**, *66*, 82–89. [CrossRef]

15. Tayeh, B.A.; Akeed, M.H.; Qaidi, S.; Bakar, B.H.A. Influence of microsilica and polypropylene fibers on the fresh and mechanical properties of ultra-high performance geopolymer concrete (UHP-GPC). *Case Stud. Constr. Mater.* **2022**, *17*, e01367. [CrossRef]
16. Xiao, R.; Huang, B.; Zhou, H.; Ma, Y.; Jiang, X. A state-of-the-art review of crushed urban waste glass used in OPC and AAMs (geopolymer): Progress and challenges. *Clean. Mater.* **2022**, *4*, 100083. [CrossRef]
17. Liew, K.M.; Sojobi, A.O.; Zhang, L.W. Green concrete: Prospects and challenges. *Constr. Build. Mater.* **2017**, *156*, 1063–1095. [CrossRef]
18. Ge, X.; Hu, X.; Shi, C. Mechanical properties and microstructure of circulating fluidized bed fly ash and red mud-based geopolymer. *Constr. Build. Mater.* **2022**, *340*, 127599. [CrossRef]
19. Althoey, F.; Zaid, O.; Alsharari, F.; Yosri, A.M.; Isleem, H.F. Evaluating the impact of nano-silica on characteristics of self-compacting geopolymer concrete with waste tire steel fiber. *Arch. Civ. Mech. Eng.* **2022**, *23*, 48. [CrossRef]
20. Aslam, F.; Zaid, O.; Althoey, F.; Alyami, S.H.; Qaidi, S.M.A.; de Prado Gil, J.; Martínez-García, R. Evaluating the influence of fly ash and waste glass on the characteristics of coconut fibers reinforced concrete. *Struct. Concr.* **2023**, *24*, 2440–2459. [CrossRef]
21. Althoey, F.; Zaid, O.; Majdi, A.; Alsharari, F.; Alsulamy, S.; Arbili, M.M. Effect of fly ash and waste glass powder as a fractional substitute on the performance of natural fibers reinforced concrete. *Ain Shams Eng. J.* **2023**, 102247. [CrossRef]
22. Alrshoudi, F.; Abbas, H.; Abadel, A.; Albidah, A.; Altheeb, A.; Al-Salloum, Y. Compression behavior and modeling of FRP-confined high strength geopolymer concrete. *Constr. Build. Mater.* **2021**, *283*, 122759. [CrossRef]
23. Wei, Y.; Jiang, C.; Wu, Y.F. Confinement effectiveness of circular concrete-filled steel tubular columns under axial compression. *J. Constr. Steel Res.* **2019**, *158*, 15–27. [CrossRef]
24. Han, L.H.; Li, W.; Bjorhovde, R. Developments and advanced applications of concrete-filled steel tubular (CFST) structures: Members. *J. Constr. Steel Res.* **2014**, *100*, 211–228. [CrossRef]
25. Shi, X.S.; Wang, Q.Y.; Zhao, X.L.; Collins, F.G. Structural behaviour of geopolymeric recycled concrete filled steel tubular columns under axial loading. *Constr. Build. Mater.* **2015**, *81*, 187–197. [CrossRef]
26. Lu, Y.; Li, N.; Li, S. Behavior of FRP-confined concrete-filled steel tube columns. *Polymers* **2014**, *6*, 1333–1349. [CrossRef]
27. Abadel, A.A.; Khan, M.I.; Masmoudi, R. Experimental and numerical study of compressive behavior of axially loaded circular ultra-high-performance concrete-filled tube columns. *Case Stud. Constr. Mater.* **2022**, *17*, e01376. [CrossRef]
28. Ombres, L.; Mazzuca, P.; Verre, S. Effects of Thermal Conditioning at High Temperatures on the Response of Concrete Elements Confined with a PBO-FRCM Composite System. *J. Mater. Civ. Eng.* **2021**, *34*, 04021413. [CrossRef]
29. Zaid, O.; Mukhtar, F.M.; M-García, R.; El Sherbiny, M.G.; Mohamed, A.M. Characteristics of high-performance steel fiber reinforced recycled aggregate concrete utilizing mineral filler. *Case Stud. Constr. Mater.* **2022**, *16*, e00939. [CrossRef]
30. Zaid, O.; Martínez-García, R.; Abadel, A.A.; Fraile-Fernández, F.J.; Alshaikh, I.M.H.; Palencia-Coto, C. To determine the performance of metakaolin-based fiber-reinforced geopolymer concrete with recycled aggregates. *Arch. Civ. Mech. Eng.* **2022**, *22*, 114. [CrossRef]
31. Maglad, A.M.; Zaid, O.; Arbili, M.M.; Ascensão, G.; Șerbănoiu, A.A.; Grădinaru, C.M.; García, R.M.; Qaidi, S.M.A.; Althoey, F.; de Prado-Gil, J. A Study on the Properties of Geopolymer Concrete Modified with Nano Graphene Oxide. *Buildings* **2022**, *12*, 1066. [CrossRef]
32. Althoey, F.; Zaid, O.; de-Prado-Gil, J.; Palencia, C.; Ali, E.; Hakeem, I.; Martínez-García, R. Impact of sulfate activation of rice husk ash on the performance of high strength steel fiber reinforced recycled aggregate concrete. *J. Build. Eng.* **2022**, *54*, 104610. [CrossRef]
33. Jiang, C. Strength enhancement due to FRP confinement for coarse aggregate-free concretes. *Eng. Struct.* **2023**, *277*, 115370. [CrossRef]
34. Zhou, W.; Feng, P.; Yang, J.Q. Advances in coral aggregate concrete and its combination with FRP: A state-of-the-art review. *Adv. Struct. Eng.* **2020**, *24*, 1161–1181. [CrossRef]
35. Abadel, A.; Abbas, H.; Albidah, A.; Almusallam, T.; Al-Salloum, Y. Effectiveness of GFRP strengthening of normal and high strength fiber reinforced concrete after exposure to heating and cooling. *Eng. Sci. Technol. Int. J.* **2022**, *36*, 101147. [CrossRef]
36. Zhong, Y.; Jiang, K.; Zhao, O. Post-fire behaviour and capacity of high strength concrete-filled high strength steel tube (HCFHST) stub columns under combined compression and bending. *Eng. Struct.* **2022**, *253*, 113837. [CrossRef]
37. Ekmekyapar, T.; Alwan, O.H.; Hasan, H.G.; Shehab, B.A.; AL-Eliwi, B.J.M. Comparison of classical, double skin and double section CFST stub columns: Experiments and design formulations. *J. Constr. Steel Res.* **2019**, *155*, 192–204. [CrossRef]
38. Phan, D.H.H.; Patel, V.I.; Liang, Q.Q.; Al Abadi, H.; Thai, H.-T. Numerical investigations of circular double-skin steel tubular slender beam-columns filled with ultra-high-strength concrete. *Eng. Struct.* **2022**, *254*, 113814. [CrossRef]
39. Lu, H.; Han, L.-H.; Zhao, X.-L. Fire performance of self-consolidating concrete filled double skin steel tubular columns: Experiments. *Fire Saf. J.* **2010**, *45*, 106–115. [CrossRef]
40. Chen, J.; Liu, Y.; Zou, M. Home location profiling for users in social media. *Inf. Manag.* **2016**, *53*, 135–143. [CrossRef]
41. Sulthana, U.M.; Jayachandran, S.A. Axial Compression Behaviour of Long Concrete Filled Double Skinned Steel Tubular Columns. *Structures* **2017**, *9*, 157–164. [CrossRef]
42. Chung, S.-K.; Kim, S.; Lee, S.-H.; Choi, S.-M. Fire Resistance of Concrete Filled Double Skin Tubular Columns under Axial Load. *J. Korean Soc. Steel Constr.* **2011**, *23*, 51–59.
43. Lu, G.-B.; Zhou, X.-H.; Wang, Y.-H.; Deng, X.-W.; Bai, Y.-T.; Zhu, R.-H. Numerical investigation on circular concrete-filled double skin steel tube columns under torsion. *Structures* **2022**, *37*, 17–31. [CrossRef]

44. Li, W.; Chen, B.; Han, L.-H.; Lam, D. Experimental study on the performance of steel-concrete interfaces in circular concrete-filled double skin steel tube. *Thin-Walled Struct.* **2020**, *149*, 106660. [CrossRef]
45. Liang, W.; Dong, J.; Wang, Q. Mechanical behaviour of concrete-filled double-skin steel tube (CFDST) with stiffeners under axial and eccentric loading. *Thin-Walled Struct.* **2019**, *138*, 215–230. [CrossRef]
46. Wang, Y.-H.; Lu, G.-B.; Zhou, X.-H. Experimental study of the cyclic behavior of concrete-filled double skin steel tube columns subjected to pure torsion. *Thin-Walled Struct.* **2018**, *122*, 425–438. [CrossRef]
47. El-Sayed, T.A. Axial Compression Behavior of Ferrocement Geopolymer HSC Columns. *Polymers* **2021**, *13*, 3789. [CrossRef]
48. Singh, B.; Ishwarya, G.; Gupta, M.; Bhattacharyya, S.K. Geopolymer concrete: A review of some recent developments. *Constr. Build. Mater.* **2015**, *85*, 78–90. [CrossRef]
49. Cong, P.; Cheng, Y. Advances in geopolymer materials: A comprehensive review. *J. Traffic Transp. Eng.* **2021**, *8*, 283–314. [CrossRef]
50. Khater, H.M.; Abd el Gawaad, H.A. Characterization of alkali activated geopolymer mortar doped with MWCNT. *Constr. Build. Mater.* **2016**, *102*, 329–337. [CrossRef]
51. Ozbakkaloglu, T.; Xie, T. Geopolymer concrete-filled FRP tubes: Behavior of circular and square columns under axial compression. *Compos. Part B Eng.* **2016**, *96*, 215–230. [CrossRef]
52. Zhang, H.Y.; Kodur, V.; Qi, S.L.; Cao, L.; Wu, B. Development of metakaolin–fly ash based geopolymers for fire resistance applications. *Constr. Build. Mater.* **2014**, *55*, 38–45. [CrossRef]
53. *ASTM E8/E8M-09*; Test Methods for Tension Testing of Metallic Materials. American Society for Testing and Materials: West Conshohocken, PA, USA, 2009. [CrossRef]
54. *ASTM D3039/D3039M-08*; Standard Test Method for Tensile Properties of Polymer Matrix Composite Materials. American Society for Testing and Materials: West Conshohocken, PA, USA, 2008.
55. Yilmaz, B.C.; Binbir, E.; Guzelbulut, C.; Yildirim, H.; Celik, O.C. Circular concrete-filled double skin steel tubes under concentric compression: Tests and FEA parametric study. *Compos. Struct.* **2023**, *309*, 116765. [CrossRef]
56. Ziemian, R.D. *Guide to Stability Design Criteria for Metal Structures*; Wiley: Hoboken, NJ, USA, 2010.
57. *ACI-308R-01-R08*; Guide to Curing Concrete. ACI: Farmington Hills, MI, USA, 2008.
58. *ASTM-C31*; Test Method for Making and Curing Concrete Test Specimens in the Field. ASTM International: West Conshohocken, PA, USA, 2017.
59. *ASTM C39*; Standard Test Method for Compressive Strength of Cylindrical Concrete Specimens. American Society for Testing and Materials: West Conshohocken, PA, USA, 2021.
60. *ASTM C496-96*; Standard Test Method for Splitting Tensile Strength of Cylindrical Concrete Specimens. ASTM International: West Conshohocken, PA, USA, 2008.
61. Ismail, I.; Bernal, S.A.; Provis, J.L.; San Nicolas, R.; Hamdan, S.; van Deventer, J.S.J. Modification of phase evolution in alkali-activated blast furnace slag by the incorporation of fly ash. *Cem. Concr. Compos.* **2014**, *45*, 125–135. [CrossRef]
62. Ostrowski, K.; Dudek, M.; Sadowski, Ł. Compressive behaviour of concrete-filled carbon fiber-reinforced polymer steel composite tube columns made of high performance concrete. *Compos. Struct.* **2020**, *234*, 111668. [CrossRef]
63. Ellobody, E.; Young, B.; Lam, D. Behaviour of normal and high strength concrete-filled compact steel tube circular stub columns. *J. Constr. Steel Res.* **2006**, *62*, 706–715. [CrossRef]
64. Fakharifar, M.; Chen, G. FRP-confined concrete filled PVC tubes: A new design concept for ductile column construction in seismic regions. *Constr. Build. Mater.* **2017**, *130*, 1–10. [CrossRef]
65. *ABAQUS UA*, version 6.19; Dassault Systèmes Simulia Corporation: Providence, RI, USA, 2019.
66. Sharif, A.M.; Al-Mekhlafi, G.M.; Al-Osta, M.A. Structural performance of CFRP-strengthened concrete-filled stainless steel tubular short columns. *Eng. Struct.* **2019**, *183*, 94–109. [CrossRef]
67. Lubliner, J.; Oliver, J.; Oller, S.; Oñate, E. A plastic-damage model for concrete. *Int. J. Solids Struct.* **1989**, *25*, 299–326. [CrossRef]
68. Lee, J.; Fenves, G.L. Plastic-Damage Model for Cyclic Loading of Concrete Structures. *J. Eng. Mech.* **1998**, *124*, 892–900. [CrossRef]
69. Comite Euro-International Du Beton. *CEB-FIP Model Code 1990: Design Code*; Thomas Telford Publishing: London, UK, 1993. [CrossRef]
70. Alshaikh, I.M.H.; Bakar, B.H.A.; Alwesabi, E.A.H.; Zeyad, A.M.; Magbool, H.M. Finite element analysis and experimental validation of progressive collapse of reinforced rubberized concrete frame. *Structures* **2021**, *33*, 2361–2373. [CrossRef]
71. Alshaikh, I.M.H.; Abadel, A.A.; Sennah, K.; Nehdi, M.L.; Tuladhar, R.; Alamri, M. Progressive Collapse Resistance of RC Beam–Slab Substructures Made with Rubberized Concrete. *Buildings* **2022**, *12*, 1724. [CrossRef]
72. *ACI Commitee 318*; Building Code Requirements for Structural Concrete and Commentary. American Concrete Institute: Farmington Hills, MI, USA, 2011.
73. Al-Mekhlafi, G.M.; Al-Osta, M.A.; Sharif, A.M. Behavior of eccentrically loaded concrete-filled stainless steel tubular stub columns confined by CFRP composites. *Eng. Struct.* **2020**, *205*, 110113. [CrossRef]
74. Wang, J.-Y.; Yang, Q.-B. Investigation on compressive behaviors of thermoplastic pipe confined concrete. *Constr. Build. Mater.* **2012**, *35*, 578–585. [CrossRef]